



HAL
open science

Performance vs. spectral properties for single-sideband continuous phase modulation

K. Kassan, Haïfa Farès, D. Christian Glattli, Yves Louët

► **To cite this version:**

K. Kassan, Haïfa Farès, D. Christian Glattli, Yves Louët. Performance vs. spectral properties for single-sideband continuous phase modulation. *IEEE Transactions on Communications*, 2021, 69 (7), pp.4402-4416. 10.1109/TCOMM.2021.3073792 . hal-03268769

HAL Id: hal-03268769

<https://hal.science/hal-03268769>

Submitted on 30 Jun 2021

HAL is a multi-disciplinary open access archive for the deposit and dissemination of scientific research documents, whether they are published or not. The documents may come from teaching and research institutions in France or abroad, or from public or private research centers.

L'archive ouverte pluridisciplinaire **HAL**, est destinée au dépôt et à la diffusion de documents scientifiques de niveau recherche, publiés ou non, émanant des établissements d'enseignement et de recherche français ou étrangers, des laboratoires publics ou privés.

Performance vs. Spectral Properties For Single-Sideband Continuous Phase Modulation

Karim Kassan, Haïfa Farès, D. Christian Glattli and Yves Louët

Abstract—This study revokes the performance of continuous phase modulation (CPM) able to generate a single-sideband (SSB) spectrum directly. This signal is analyzed in terms of modulation indices, pulse lengths, and pulse widths, all of which affect error probability, bandwidth, SSB property, and receiver complexity. The error probability performance is based on an approximation of the minimum Euclidean distance. A numerical power spectral density calculation for this particular SSB modulation in terms of the modulation index is presented. Reasonable tradeoffs in designing modulation schemes have been proposed using multi-objective optimization to ensure sizable improvements in bit error rate (BER), spectral efficiencies, and complexity without losing the property of being a SSB signal. Performance comparisons are made with known CPM schemes, e.g., Gaussian Minimum Shift Keying (GMSK) and Raised Cosine based CPM (RC).

Index Terms—Continuous phase modulation (CPM), maximum likelihood sequence detection (MLSD), minimum Euclidean distance, power spectral density (PSD), single-sideband (SSB).

I. INTRODUCTION

CONTINUOUS phase modulation (CPM) schemes [1] are particularly suitable for long-distance wireless communications due to high energy efficiency resulting from their constant signal envelopes. Many digital communication systems use the CPM family, e.g., satellite and deep-space communications, optical fiber, telemetry, etc. Recently, the authors of [2] proposed a CPM scheme, which has the original feature of directly generating a single-sideband (SSB) spectrum, which in turn, provides a highly compact frequency occupancy. By *directly*, we mean that SSB property results from the original modulation and not from post-filtering [3]. This waveform is hereafter referred to as Single-Sideband Frequency Shift Keying (SSB-FSK). SSB-FSK uses a generic phase derivative pulse with a *Lorentzian* shape and a 2π phase increment. The Lorentzian pulse belongs to specific shapes addressing fundamental quantum physics, particularly the on-demand injection of a single electron in a quantum conductor. Digital communications based on CPM were the first immediate application of *classical levitonics* [4]. In [3], we presented the principle of the modulation and its mathematical justification. However, we did not provide any result about detection schemes or the interplay between error probability performance, bandwidth, and SSB property. Besides, CPM signals suffer from receiver complexity due to the memory property introduced by the phase continuity, which should also be considered alongside the error probability, bandwidth, and

SSB property. In this paper, we suggest several tradeoffs under all these considerations to get the full potential of SSB-FSK signals.

A. Related Work On Single-Sideband CPM

SSB-FSK originates from the theoretical proposal of Levitov *et al.* [5], who demonstrated how to create a pure single electron without any perturbation in the quantum conductor. It is widely accepted that a quantum conductor is full of many free-moving electrons. When one electron is excited by an elementary pulse, others tend to move to fill the hole created, generating undesirable neutral plasmonic waves. To overcome this issue, Levitov *et al.* predicted that one could inject an electron without causing any disturbance *if and only if* the voltage pulse follows a Lorentzian time shape. Using the Lorentzian pulse, we can generate a pure single electron state, called a “Leviton”, a new quasi-particle with minimal excitation. As a consequence it has been shown in [6], and [7], that the electron energy distribution become SSB, i.e., its left part is removed. Based on this experimentation, the authors in [4] proposed a new CPM modulation scheme, which directly provides a SSB signal. Then in [2] and [8], we provided the first system model of SSB-FSK as a CPM modulation.

Additionally, we introduced some properties, such as the symbol-by-symbol coherent demodulation scheme, based on SSB-FSK signals’ orthogonality. Due to the memory effect characterizing the CPM signals, we developed an average matched filter detector, making decisions according to a given observation window. We then analyzed the power spectral density (PSD) for the binary case, leading us to demonstrate that the SSB-FSK signal’s PSD is unilateral with respect to the carrier frequency (f_c), and almost all of the power is concentrated in the first period of the frequency band. Finally, in [3], we presented an analytical expression of the power spectral density (PSD) for binary and quaternary SSB-FSK.

B. Main Contributions

In this paper, we report a complete study of the SSB-FSK performance regarding error probability, spectral efficiency, complexity, and SSB property depending on the following parameters:

- Modulation index h : even if increasing h consistently increases the bandwidth (BW) occupancy, it does not carry a monotonic impact on the error probability performance and the SSB property.
- Pulse length L : increasing L results in a complete response of the Lorentzian filter and will introduce a better BW occupancy and lower side lobes, although the more significant L , the larger the receiver complexity.

K. Kassan, H. Farès and Y. Louët are with IETR - UMR CNRS 6164, CentraleSupélec Rennes Campus, avenue de la Boulaie - CS 47601 35576 CESSON-SEVIGNE Cedex, France (e-mail: karim.kassan@ieee.org {haifa.fares, yves.louet}@centralesupelec.fr).

D. C. Glattli is with SPEC UMR 3680 CEA-CNRS, Université Paris-Saclay, CEA-Saclay, 91191 Gif-Sur-Yvette, France (e-mail: christian.glattli@cea.fr).

- Modulation level size M : an increment in M produces a gain in error probability performance while degrading the BW occupancy and increasing complexity.
- Pulse width w : it is a new tuning parameter introduced especially for SSB-FSK, which plays an essential role in error probability and BW occupancy performance.

It is worth emphasizing the need for a functional interplay between all these parameters, which leads to opposite effects on the error probability, spectral efficiency, complexity, and SSB property. Therefore, we need to define certain tradeoffs between these parameters as long as an optimal scheme considering all performance metrics is impossible.

The four key contributions of this paper are:

- 1) The study of the Maximum Likelihood Sequence Detector (MLSD) performance on the SSB-FSK signals and the effects of all parameters (h, w, L, M) on the error probability performance—mainly the effect of pulse width w . Additionally, we highlight some points related to memory performed by the Viterbi algorithm [9]. We gave the error probability performance in terms of an approximation of the achievable minimum Euclidean distance.
- 2) The study of the effect of all parameters (h, w, L, M) on the power spectral density (PSD): this study is mainly performed for $h \neq 1$, and its results have been compared to those obtained from the particular case of $h = 1$ (responsible of pure SSB signal and particularly relevant for synchronization purpose) [2].
- 3) A method to select the best parameter combinations to obtain the optimal performance of the SSB-FSK scheme; this method is based on the *Pareto optimum*, which is a multi-objective optimization method. This study is done in two steps: first, the optimization is performed without constraints on the receiver's complexity. Second, the complexity is considered as the third objective function, alongside energy efficiency and bandwidth occupancy.
- 4) Energy-bandwidth comparisons for SSB-FSK signals. We were able to define some configurations with acceptable tradeoffs between energy consumption, BW occupancy, and complexity for SSB-FSK, which outperform popular CPM schemes (e.g., GMSK, RC). We also present a new SSB-FSK configuration with an integer modulation index h that combines good performance and synchronization advantage.

The rest of the paper is organized as follows. In Section II, we briefly introduce the signal model. In Section III, we evaluate the error probability performance of SSB-FSK signals using the union bound. In Section IV, we present a numerical method to compute the PSD using the autocorrelation approach. In Section V, we present the *Pareto optimum*, a multi-objective optimization method, which is used alongside a *brute force* method to obtain the best possible tradeoffs for the SSB-FSK scheme. In Section VI, we illustrate several simulation results for error probability performance, power spectrum performance, energy-bandwidth comparison, and synchronization advantage, respectively. Finally, the main outcomes of this study in terms of concluding remarks and design directives are

TABLE I:
Table of symbols.

Symbol	Indication
h, \tilde{h}	CPM modulation index, SSB-FSK CPM modulation index
L	Pulse length
M	Modulation level
w	Pulse width
BW	Bandwidth occupancy
α	Transmitted symbol
E_s, T_s	Energy per transmitted symbol, Duration of the transmitted symbol
μ	2π phase increment correcting factor
d_{\min}^2, d_B^2	Minimum squared Euclidean distance, Minimum squared Euclidean distance upper bound
N	Number of observation symbols
γ	Difference data sequence
P_k	Priori probabilities of the data symbols
N_s	Number of states needed to implement the MLSD receiver

summarized in Section VII. Conclusions are drawn in Section VIII.

II. SINGLE-SIDEBAND CPM SYSTEM MODEL

The SSB-FSK signal is defined as CPM [1] with the complex representation

$$s(t, \alpha) = \sqrt{\frac{E_s}{T_s}} \exp \left\{ j\phi(t; \alpha) \right\}, \quad (1)$$

where E_s is the energy per transmitted symbol and T_s is the duration of the symbol. The information-carrying phase is defined as

$$\phi(t, \alpha) = 2\pi\tilde{h} \sum_{i=-\infty}^{+\infty} \alpha_i \phi_0(t - iT_s) \quad (2)$$

where α_i is the transmitted symbol that takes values from the M -ary level $0, 1, \dots, (M-1)$. In order to preserve the SSB property, we have to consider positive symbols α_i , responsible of the right side band spectrum. The negative values would introduce a lower side in the spectrum. Therefore, no antipodal coding is allowed [2, 8]. Furthermore, $\tilde{h} = 2h$, where h is the modulation index used to ensure a 2π phase increment. The phase response $\phi_0(t)$ is represented as

$$\phi_0(t) = \begin{cases} 0 & t < 0 \\ \frac{1}{4\pi} \int_{-\infty}^t g(\tau) d\tau & 0 \leq t < LT_s \\ \frac{1}{2} & t \geq LT_s \end{cases} \quad (3)$$

where $g(t)$ is a Lorentzian frequency pulse truncated to a symbol duration $L > 1$ (*partial-response*), defined as

$$g(t) = \frac{d\phi_0(t)}{dt} = \mu \frac{2w^2}{t^2 + w^2}, \quad (4)$$

$$t \in [-LT_s/2, LT_s/2].$$

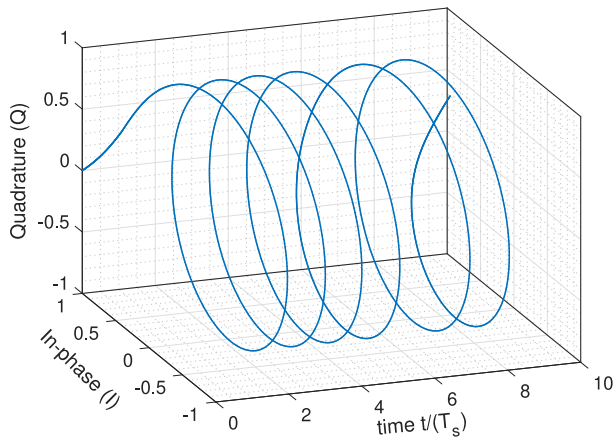


Fig. 1: Generated SSB-FSK signal with $L = 4$, $w = 0.3$ and $h = 1$ of the bits sequence $\{1, 1, 1, 1, 0, 1, 1, 0, 0, 1\}$.

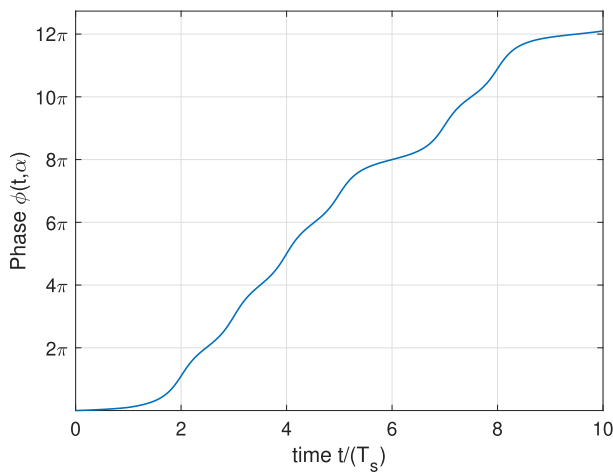


Fig. 2: Evolution of the phase $\phi(t, \alpha)$ with $L = 4$, $w = 0.3$ and $h = 1$ of the bits sequence $\{1, 1, 1, 1, 0, 1, 1, 0, 0, 1\}$.

The variable w is the pulse width, a key tuning parameter that significantly impacts the performance, mainly the transmitted signal's spectral efficiency $s(t, \alpha)$ [2, 8].

Fig. 1 shows the constant envelope of the SSB-FSK modulated signal in the time domain; Fig. 2 depicts the continuity of SSB-FSK phase.

As a slow decrease characterizes the Lorentzian pulse, a pulse truncation is needed to get acceptable pulse lengths (regarding especially receiver complexity). As a consequence a correcting factor μ is introduced to keep a 2π phase increment to sustain the SSB property. The correcting factor μ is defined as the ratio between the total phase increment without any truncation and the one obtained after Lorentzian truncation:

$$\mu(L) = \frac{2\pi}{\int_{-LT_s/2}^{LT_s/2} \frac{2w^2}{t^2+w^2} dt} = \frac{\pi}{2 \arctan(\frac{LT_s}{2w})}. \quad (5)$$

The effect of w on the frequency pulse $g(t)$ for $L = 4$ is presented in Fig. 3, for different values of $w = 0.3, 0.7, 1.3$. As shown in Fig. 3, it is evident that increasing w brings up the tails of frequency pulse $g(t)$, which consequently increases the inter-symbol interference (ISI).

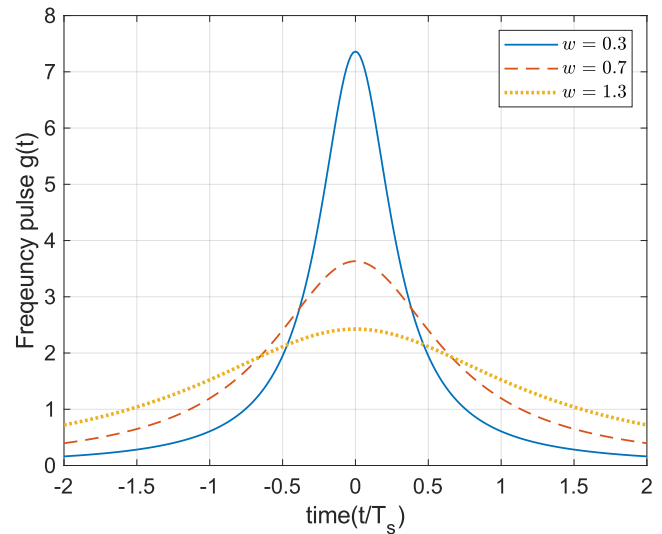


Fig. 3: Lorentzian pulse ($L=4$) for different width values, $w = 0.3, 0.7, 1.3$.

III. SINGLE-SIDEBAND CPM ERROR PROBABILITY

In this section, we consider the performance of SSB-FSK when transmitted over an additive white Gaussian noise (AWGN) channel, assuming there is no channel coding. To evaluate the signal's performance, we used the same method shown in [1, Ch. 3]. We consider the union bound of the error probability as the asymptotic performance for high values of E_b/N_0 , where E_b is the mean energy per information bit. The union bound is defined as in [1, Ch. 3, p. 55]

$$P_e \sim Q\left(\sqrt{d_{\min}^2 \frac{E_b}{N_0}}\right), \quad (6)$$

where d_{\min}^2 is the minimum squared Euclidean distance. The function $Q(\cdot)$ is the error Gaussian function defined by

$$Q(x) = \int_x^{+\infty} \frac{1}{\sqrt{2\pi}} e^{-v^2/2} dv. \quad (7)$$

The normalized squared Euclidean distance (d^2) is the Euclidean difference between any two transmitted SSB-FSK data sequences α and α' . The general form of the normalized squared Euclidean distance for any set of signals is given by

$$d^2(\alpha, \alpha') = \frac{1}{2E_b} \int_0^{NT_s} |s(t, \alpha) - s(t, \alpha')|^2 dt, \quad (8)$$

where NT_s is the observation symbol interval length. The normalized squared Euclidean distance $d^2(\alpha, \alpha')$ can be represented as a function of a single difference data sequence γ , where $\gamma = \alpha - \alpha'$. Therefore, (8) can be rewritten as (see appendix A for the derivation details)[1, ch.2]

$$d^2(\gamma) = \log_2 M \left\{ N - \frac{1}{T_s} \int_0^{NT_s} \cos[\phi(t, \gamma_N)] dt \right\}, \quad (9)$$

where $\phi(t, \gamma_N)$ is the phase difference trajectories.

To calculate the minimum normalized squared Euclidean distance (d_{\min}^2) for N observation symbols, we need to find pairs of γ that minimize (9). It is clear that (9) has a positive

integral, which means that the higher the N we observe, the higher the Euclidean distance we obtain. Consequently, if we obtain an upper bound for N converging to infinity, we obtain an upper bound for any defined N . This suggests the search for the difference phase trajectories $\phi(t, \gamma)$ with the shortest duration time τ , where $\phi(t, \gamma)$ is equal to zero at all times $t \geq \tau$. Hence, an upper bound (d_B^2) on the Euclidean distance $d^2(\gamma)$ can be obtained using only $\phi(t, \gamma)$ with the shortest length τ . To better clarify the idea, we use in Fig. 4 the difference phase tree for any modulation index h to illustrate the method we used to obtain the boundary. Since we are presenting different phase trees, the first symbol γ_0 cannot be zero where α_0 and α'_0 must not be the same. Using the difference phase tree, we can evaluate γ with the shortest length of τ . We search for the merger points between two different paths using the different phase trajectories ($\phi(t, \gamma)$) that start at $t = 0$, and coincide with the x-axis at a certain time $t = t_m$, and coincide after for $t > t_m$. In Fig. 4, we showed two of the merger points A and B, and two of the best γ combinations with the shortest τ (presented as marked lines). We can directly see that the difference phase tree with the best γ combinations (presented as marked lines) coincide at t equal to 4 and 5 with the x-axis, respectively, at the points A and B, and continue to be aligned with the x-axis from these points to the end. Usually, the time instant of the first merger point is obtained at $t = (L + 1)T_s$, for non-weak modulation schemes [1, Ch. 3, p. 73]. The phase difference tree, with the best difference sequence γ , is defined by

$$\gamma_i = \begin{cases} 0 & i < 0 \\ 1, 2, \dots, (M - 1), & i = 0 \\ 0, \pm 1, \pm 2, \dots, \pm(M - 1), & 0 < i < m + 1 \\ 0 & i \geq m + 1 \end{cases}, \quad (10)$$

given that

$$\sum_{i=0}^m \gamma_i = 0. \quad (11)$$

The variable m is the merger point index; the higher the number of mergers we select, the tighter the upper bound d_B^2 we obtain (in Fig. 4, we showed only the first and the second merger points A and B, which corresponds to $m = 1$ and $m = 2$ respectively). As the exact number of mergers is not known [1, Ch. 3, p. 74], the number of mergers is selected by trial and is increased until there is no change in the upper bound d_B^2 , given that there is no case where mergers later than the L^{th} needed [1, Ch. 3, p. 74].

The calculation of d_{\min}^2 is obtained using the sequential search algorithm proposed in [10]. The search algorithm requires the upper bound d_B^2 ; the main objective of the upper bound d_B^2 is to accelerate the algorithm search. For instance, any pair of phase trajectories with the corresponding γ_N for specific h and w values, having a distance value defined in (9) larger than d_B^2 , will not be used again. The steps to obtain the minimum normalized squared Euclidean distance (d_{\min}^2) are summarized below:

- **Step 1:** select the merger point index m .

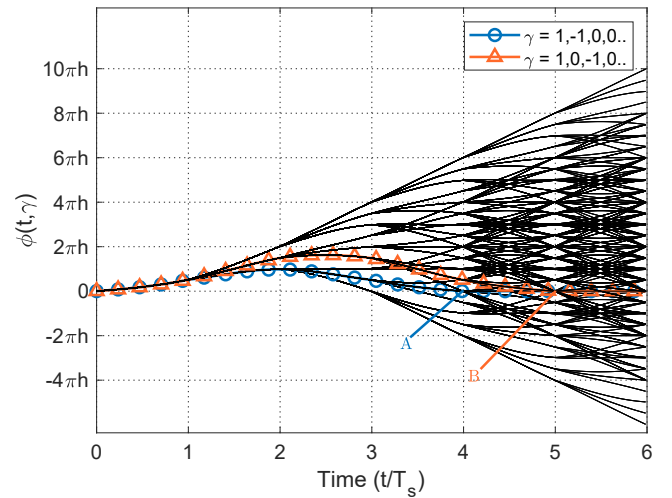


Fig. 4: Phase difference tree for binary SSB-FSK with $L = 3$ and $w = 0.9$. A and B indicate mergers.

- **Step 2:** use exhaustive search to calculate the set S_γ of difference sequences γ according to (10) and (11).
- **Step 3:** compute $d^2(\gamma)$ based on (9) for each difference sequence obtained in the set S_γ .
- **Step 4:** the upper bound of the minimum distance d_B^2 is equal to the minimum bound of all normalized squared Euclidean distance obtained from **step 3** ($d_B^2 = \min_{\gamma \in S_\gamma} d^2(\gamma)$).
- **Step 5:** calculate d_{\min}^2 from the algorithm presented in [10], using the d_B^2 obtained from **step 4**.

IV. SINGLE-SIDEBAND CPM POWER SPECTRUM

The spectrum occupancy plays an essential role in the overall performance of the transmitted signal, as it is a limited resource. Therefore, it is important to minimize the usage of this resource as much as possible. In this section, we apply a numerical method to compute the power spectral density and, consequently, analyze the SSB-FSK signals' spectrum efficiency for different parameters (h, L, w, M). The method is based on [1, Ch. 4] [11] and [12, Ch. 3], which is a generalization of the solution developed by Greenstein for time-limited phase response CPM signals [13].

A. Non-Integer Modulation Index

The method used in [1, Ch. 4] [11] and [12, Ch. 3] for the power spectrum calculation is based on the evaluation of the autocorrelation of the Fourier transform function, given that $s(t, \alpha)$ is cyclostationary. Therefore, we first introduce the autocorrelation function, where we assume a baseband signal, given by

$$\begin{aligned} R(\tau) &= R(\tau' + mT_s) \\ &= \frac{1}{T_s} \int_0^{T_s} \prod_{i=1-L}^{m+1} \left\{ \sum_{k=0}^{M-1} P_k \exp(j2\pi hk \right. \\ &\quad \left. [\phi_0(t + \tau' - (i - m)T_s) - \phi_0(t - iT_s)] \right\} dt. \end{aligned} \quad (12)$$

The variable $\tau = \tau' + mT_s$ is the time difference over the interval $[0, (L+1)T_s]$, with $0 \leq \tau' < T_s$ and $m = 0, 1, 2, \dots$. The variable P_k is a priori probability of the data symbol k . The PSD is obtained by using the Fourier transform of (12), given by

$$S(f) = 2 \Re \left\{ \int_0^{LT_s} R(\tau) e^{-j2\pi f\tau} d\tau + e^{-j2\pi fLT_s} \sum_{m=0}^{\infty} C_\alpha^m e^{-j2\pi fmT_s} \int_0^{T_s} R(\tau + LT_s) e^{-j2\pi f\tau} d\tau \right\}, \quad (13)$$

where

$$C_\alpha = \sum_{k=0}^{M-1} P_k e^{jh\pi k} \quad (14)$$

for h values for which $|C_\alpha| < 1$. The summation in (13) converges, leading to

$$\sum_{m=0}^{\infty} C_\alpha^m e^{-j2\pi fmT_s} = \frac{1}{1 - C_\alpha e^{-j2\pi fT_s}}. \quad (15)$$

Inserting (15) into (13), we obtain the PSD expression given by

$$S(f) = 2 \Re \left\{ \int_0^{LT_s} R(\tau) e^{-j2\pi f\tau} d\tau + \frac{e^{-j2\pi fLT_s}}{1 - C_\alpha e^{-j2\pi fT_s}} \int_0^{T_s} R(\tau + LT_s) e^{-j2\pi f\tau} d\tau \right\}. \quad (16)$$

However, this PSD equation (16) is only valid for $|C_\alpha| < 1$, i.e., for non-integer h . Therefore, in Subsection IV-B, we apply certain modifications to obtain the PSD for integer h .

B. Integer Modulation Index

For $|C_\alpha| = 1$ (integer h), (15) is not valid anymore. However, with $|C_\alpha| = 1$, we can set

$$C_\alpha = e^{j2\pi v}, \quad 0 \leq v < 1. \quad (17)$$

Based on (17), the summation in (15) can be rewritten as [12, Ch. 3, p. 141]

$$\sum_{m=0}^{\infty} e^{-j2\pi T_s(f-v/T_s)m} = \frac{1}{2} + \frac{1}{2T_s} \sum_{m=-\infty}^{\infty} \delta\left(f - \frac{v}{T_s} - \frac{m}{T_s}\right) - j\frac{1}{2} \cot \pi T_s \left(f - \frac{v}{T_s}\right). \quad (18)$$

Inserting (18) into (13) leads to the complete PSD expression for integer h , which covers the spectrum's discrete and continuous components. Moreover, based on (18), the discrete spectrum spikes are located at frequencies

$$f_m = \frac{m+v}{T_s}, \quad 0 \leq v < 1. \quad m = 0, 1, 2, \dots \quad (19)$$

V. MULTI-OBJECTIVE OPTIMIZATION

SSB-FSK has several conflicting objectives that need to be optimized, where the major challenge is to find tradeoffs for designing a competitive SSB CPM-based system. We have thus divided this section into three parts:

- Objective functions: in this part, we summarize the performance metrics considered in the optimization analysis.
- Design space: a massive number of configurations have to be tested due to the variety of parameters. Therefore, it is interesting to reduce this number of combinations by excluding situations that cannot be envisaged, i.e., by defining a feasible region of the optimization problem variables.
- Optimization method: as we have several objectives to optimize, different methodologies are possible. One solution is to optimize one performance metric when considering others constrained to a certain threshold (drawn from well-known other CPM schemes). Using this methodology, we define plenty of optimization problems (as many as possible combinations between considered objective functions and fixed thresholds for constrained performance metrics). Therefore, the best course of action is to jointly optimize all performance metrics by defining several intermediate configurations leading to different tradeoffs depending on the order of priority given for these objective functions.

A. Objective Functions

- *Minimum Normalized Squared Euclidean Distance* (d_{\min}^2): it measures the energy consumption of the signals, based on the error probability bound given in (6). It is clear that an increase of d_{\min}^2 can be seen as a reduction in the mean energy per information bit E_b for the same targeted probability error.
- *Bandwidth Occupancy (BW)*: it estimates the *BW* occupancy of the signal. We divided the *BW* occupancy into two measurements; the first one computes 99% of the signal power inside BT_b , where $T_b = T_s / \log_2 M$ and B represents the total bandwidth occupancy and not half of it due to the unsymmetrical spectrum shape form of the SSB-FSK modulation. The second measurement computes 99.9% of the power inside BT_b . With the second measurement, we obtain a better idea about the out-of-band leakage. We noted these two measurements B_{99} and B_{999} , respectively. The objective of both measurements is to estimate the *BW* occupancy of BT_b . We note that the bandwidth BT_b is normalized to the data rate in terms of bits carried per second so that schemes with different modulation levels M can be compared.
- *Complexity* (N_s): it is given by the number of states used to implement the MLSD receiver [1, ch.3, p.111-p.113]:

$$N_s = \begin{cases} p & L = 1 \\ pM^{L-1} & L > 1 \end{cases}, \quad (20)$$

where p is the number of phase states obtained from the modulation index $h = \frac{2m}{p}$ (for SSB-FSK, $\tilde{h} = \frac{2m}{p}$).

- *Single-Sideband Loss* (SSB-LOSS): the SSB-LOSS is a specific objective function defined only for SSB-FSK signals (as they are the only CPM signals having this spectral feature). SSB-LOSS estimates the percentage of power loss in the lower band (the respectively upper band for negative modulation indices h) of the PSD.

Due to the enormous computational complexity of all of these metrics, we had to establish a priority order among them. Therefore, we provided the highest priority degree to the signal energy consumption, normalized BW occupancy, and complexity, where we tried to find certain tradeoffs between these three objective functions. Based on these tradeoffs, we sequentially tried to reduce the SSB-LOSS.

B. Space Design

The initial step for solving a multi-objective function is to define a feasible region for the problem. In this study, we are mainly interested in three objective functions: energy consumption, normalized BW occupancy, and complexity. Therefore, the feasible region for the constraints is discussed hereafter :

- 1) *Modulation index h* : it is important to keep a small h , where large h has a significant impact on the occupied BW [1, Ch. 4] [14, 15] (more information about the effect of h on the spectrum of SSB-FSK signals, are presented in VI-C). Therefore, we define the modulation index range $0.01 \leq h \leq 2$, with an increment step size $h_s = 0.01$.
- 2) *Pulse length L* : an increase in L will produce an increase in complexity (20) [12, ch. 4, p. 248]. Therefore, considering the values taken from the literature, L will be less than 8. [1, 16][17], where $L = 8$ is already a complex system. However, in [2], constrained by the specific slow decrease of the Lorentzian pulse, we allowed a pulse length $L = 12$. Therefore, we defined the pulse length range as $1 \leq L \leq 12$ with an increment step size $L_s = 1$. We will not exceed this maximum value of $L = 12$ to not explode the receiver complexity gaining very little on the SSB property.
- 3) *Modulation level M* : an increase in M will create an increase in complexity (20) [12, ch. 4, p. 248], and a degradation in normalized BW occupancy BT_b for the same modulation index (h) [1]. Therefore we selected M to take only discrete values $\{2, 4, 8\}$.
- 4) *Pulse width w* : w is a new parameter introduced by the SSB-FSK. Based on [2], increasing w will impact the SSB-FSK PSD exponential decrease, which can be quantified to $\exp(-4\pi w/T_b)$ for the particular case $h = 1$. Therefore, it is worth studying the effect of the pulse width w more deeply on energy computation and normalized BW occupancy BT_b . To fully cover the effect of the pulse width w , we also need to define a numerical range that covers the *useful* region (a reduced set of the *feasible* region). The pulse width w can only be found in the frequency pulse expression given by (4). It is clear from this expression that no restriction

TABLE II:

Pulse width limit w_{lim} with respect to pulse length L for binary SSB-FSK.

L	2	4	6	8	10	12
w_{lim}	1.6	3.2	4.8	6.4	7.9	9.5

are found to delimit the possible values of w (except that it has to be a non-null positive real). Therefore, to cover the entire *feasible* region, we need to consider all pulse width w values, i.e., $w \in]0, \infty[$.

Consequently, we define w_{lim} as a new limit of the pulse width w , where for $w_{\text{lim}} \leq w \leq \infty$ we obtain approximately the same frequency pulse $g(t)$. Hence, it will be possible to reduce the study to $w \in]0, w_{\text{lim}}]$, which is now the *useful* region. The calculation of w_{lim} is straightforward using the 2-norm defined as

$$\|x\|_2 = \sqrt{\sum_i |x_i|^2}. \quad (21)$$

The error is then calculated using

$$\epsilon = \frac{\|\hat{x} - x\|_2}{\|x\|_2}, \quad (22)$$

where x is the frequency pulse $g_\infty(t)$, for $w = \infty$ (in numerical simulation, we take $w = 1000$). Furthermore, \hat{x} is the estimated frequency pulse $g_{\text{lim}}(t)$, for $w = w_{\text{lim}}$. We calculate w_{lim} for each L in the defined interval. The criteria to obtain w_{lim} from (22) is to maintain an error $\epsilon \leq 10^{-1}$. In Table II, we present w_{lim} with respect to the pulse length L for binary SSB-FSK. Finally, we define the pulse width range $0.1 \leq w \leq w_{\text{lim}}$. It is worth noting that w_{lim} is increasing with respect to the pulse length L . Therefore, more configurations have to be considered when increasing L as the defined range of w is getting wider. Moreover, the increment step size is $w_s = 0.1$.

C. Optimization Method (Without Complexity)

In multi-objective problems, there is no single global optimal solution. Therefore, *Pareto optimum* is used to find all optimal points. A solution is said to be the *Pareto optimum* (P_{opt}) if there is no other solution that can improve at least one objective function without reducing the other objective functions. The objective functions in our case are

$$F(x) = [F_1(x), F_2(x)], \quad (23)$$

where

$$F(x_1) > F(x_2) \iff \forall_i F_i(x_1) > F_i(x_2). \quad (24)$$

$F_1(x)$ and $F_2(x)$ are the $10\log_{10}(d_{\text{min}}^2/2)$ and the inverse of the normalized bandwidth occupancy ($1/BT_b$), respectively. The constraints variables (h, L, M, w) are denoted here by $x \in \mathbb{R}^4$. The definition of *Pareto optimum* is given by (we present the weak *Pareto optimum*) :

$$x^* = P_{\text{opt}} \iff \nexists y \text{ such that } F(y) > F(x^*). \quad (25)$$

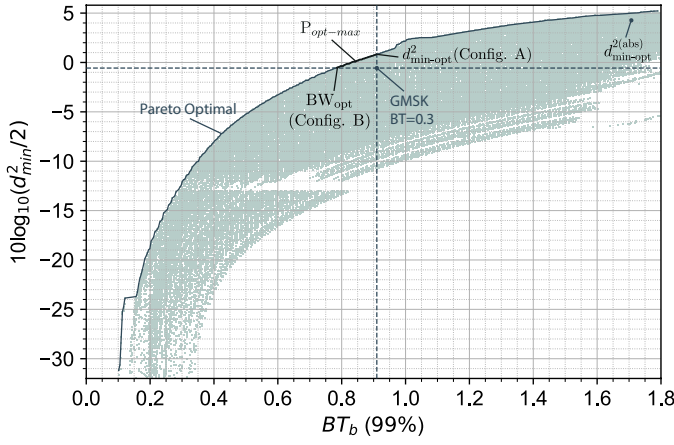


Fig. 5: Two objective functions Pareto optimum plot for binary LSSB-FSK using B_{99} . GMSK for $BT = 0.3$ is presented as a reference point.

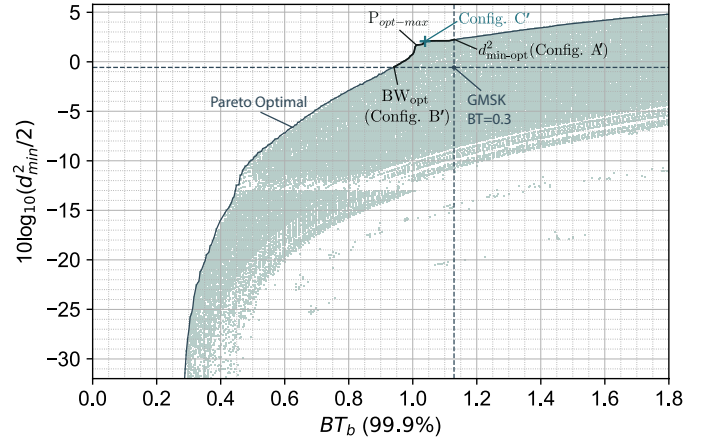


Fig. 6: Two objective functions Pareto optimum plot for binary LSSB-FSK using $B_{99.9}$. GMSK for $BT = 0.3$ is presented as a reference point.

TABLE III:

SSB-FSK optimum minimum normalized squared Euclidean distance $d_{\min-\text{opt}}^2$ and optimum normalized bandwidth occupancy BW_{opt} for 99% bandwidth BW occupancy, for different modulation levels M .

$d_{\min-\text{opt}}^2$ - Config. A							
M	L	w	h	d_{\min}^2	BW	SSB-LOSS (%)	N
2	5	1.3	0.78	2.4	0.906	1.764	15
4	2	0.7	0.49	3.53	0.906	2.561	25
8	2	0.6	0.36	3.25	0.904	1	8
BW_{opt} - Config. B							
M	L	w	h	d_{\min}^2	BW	SSB-LOSS (%)	N
2	5	1.2	0.65	1.774	0.785	2	14
4	2	0.8	0.33	1.773	0.65	2.732	10
8	2	0.6	0.26	1.8	0.677	1.21	8

TABLE IV:

SSB-FSK optimum minimum normalized squared Euclidean distance $d_{\min-\text{opt}}^2$ and optimum normalized bandwidth occupancy BW_{opt} for 99.9% bandwidth BW occupancy, for different modulation levels M .

$d_{\min-\text{opt}}^2$ - Config. A'							
M	L	w	h	d_{\min}^2	BW	SSB-LOSS (%)	N
2	12	0.8	1.04	3.346	1.129	0.366	18
4	2	0.7	0.44	2.98	1.25	2.611	7
8	2	0.7	0.35	3.025	1.114	0.955	8
BW_{opt} - Config. B'							
M	L	w	h	d_{\min}^2	BW	SSB-LOSS (%)	N
2	6	1.1	0.67	1.773	0.941	1.683	14
4	2	0.7	0.33	1.814	0.902	2.930	8
8	2	0.6	0.26	1.8	0.902	1.214	8

For more information about the *Pareto optimum*, please refer to [18, 19].

We used a *Brute Force* method to obtain all the values of $F_1(x)$ and $F_2(x)$ for the space Z , where Z is constrained by the parameters h, L, M, w and their defined ranges. Based on this *Brute Force*, we apply the *Pareto optimum* optimization to obtain all the optimum solutions for Z .

Remarks:

- We calculate the minimum normalized squared Euclidean distance (d_{\min}^2) using the algorithm introduced in Section III. We consider all the mergers for merger index $m = 3$ (the number of mergers is found by trials). Moreover, we also consider $N_{\max} = 30$, where N is the number of observation symbols.
- We calculate B_{99} and $B_{99.9}$ normalized BW occupancy (BT_b) using the method presented in Section IV. Hence, we obtain different P_{opt} for each normalized bandwidth BW occupancy BT_b measure.

Fig. 5 and Fig. 6 present the *Pareto optimum* for binary

LSSB-FSK¹ using B_{99} and $B_{99.9}$, respectively. Moreover, the GMSK performance for $BT = 0.3$ is considered here as a reference point. Hence, for this part, we consider only the Pareto front values which have a normalized bandwidth BW occupancy that is less than or equal to the GMSK bandwidth BW occupancy and a minimum normalized squared Euclidean distance d_{\min}^2 greater than or equal to the GMSK distance d_{\min}^2 . These values are illustrated in the upper left quarter of the plane delimited by the GMSK reference point's axis in Fig. 5 and Fig. 6. We will refer to these values as $P_{\text{opt-max}}$. In Fig. 5, $P_{\text{opt-max}}$ is achieved with 26 different configurations (parameter combinations). In Fig. 6, $P_{\text{opt-max}}$ is achieved with 29 different configurations. Note that each point of $P_{\text{opt-max}}$ corresponds to a particular configuration, and the number of configurations depends on the parameters step used in the search (L_s, w_s, h_s).

Table III and Table IV present the optimum minimum

¹LSSB-FSK: LSSB-FSK presents the pulse length L of SSB-FSK signal pulse, e.g., 3SSB-FSK is the SSB-FSK modulation for pulse length $L = 3$.

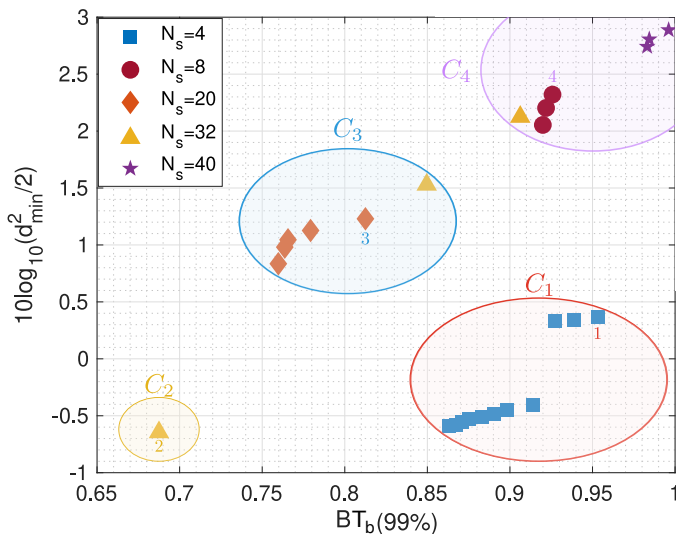


Fig. 7: Three Pareto optimum objective functions configurations for binary LSSB-FSK using B_{99} .

normalized squared Euclidean distance $d_{\min\text{-opt}}^2$ and optimum normalized bandwidth occupancy BW_{opt} for 99% and 99.9% occupancies, respectively, as a function of the SSB-FSK parameters for different modulation levels M . Considering only the $P_{\text{opt-max}}$ configurations, we have $d_{\min\text{-opt}}^2$ and BW_{opt} as the highest minimum normalized squared Euclidean distance d_{\min}^2 (higher d_{\min}^2 mean lower energy consumption), and the lowest normalized bandwidth (BW) occupancy values obtained respectively. These points are denoted by Config. A (for $d_{\min\text{-opt}}^2$) and Config. B (for BW_{opt}) for B_{99} (Config. A' and Config. B' according to B_{999}). Besides, we also show the number of observation symbol intervals N needed (the Viterbi algorithm memory highly depends on N) and the SSB-LOSS generated. The *Pareto optimum* analysis (Fig. 5 and Fig. 6) gives all possible tradeoffs combining both normalized minimum Euclidean distance d_{\min}^2 (y-axis, $10\log_{10}(d_{\min}^2/2)$) and normalized bandwidth occupancy metrics (x-axis). Table III and Table IV give absolute optimum values, performing better than the GMSK, for each performance metric *alone* and the resulting effect on the other one. Furthermore, in Fig. 6, we can see that the normalized minimum Euclidean distance d_{\min}^2 performance has a small variation between Config. A' and Config. C' (the line is quite horizontal). Therefore, Config. C' seems an interesting point (another good tradeoff) since it offers almost the same normalized minimum Euclidean distance d_{\min}^2 while significantly decreasing the normalized bandwidth BW occupancy. Config. C' corresponds to the following parameters combination ($L = 12$, $w = 0.7$, $h = 0.99$); leading to $d_{\min\text{-C}}^2 = 3.216$, $BW_{\text{C}} = 1.043$.

D. Optimization Method (With Complexity)

In this part, we consider three objective functions for optimization: $10\log_{10}(d_{\min}^2/2)$, the inverse of the normalized bandwidth occupancy ($1/BT_b$), and the number of states (N_s). Similar to Section V-C, we apply the *Pareto optimum* optimization with the three selected objective functions to

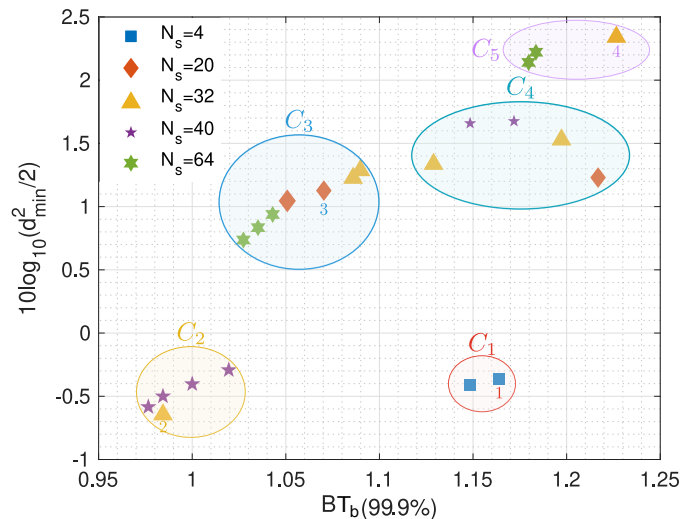


Fig. 8: Three Pareto optimum objective functions configurations for binary LSSB-FSK using $B_{99.9}$.

obtain all the optimum solutions for the space S . Unlike Z , the space S presents only the configurations with a number of states $N_s \leq 64$ (a system with $N_s > 64$ is considered to be very complex). Moreover, the configurations in space S can have energy ($10\log_{10}(d_{\min}^2/2)$) values higher or equal to the GMSK energy minus “0.1”, and a normalized bandwidth occupancy BW lower or equal to GMSK BW plus “0.1”.

In Fig. 7 and Fig. 8, we illustrate the configurations obtained from the three objectives *Pareto Optimum* optimization, respectively, for B_{99} and $B_{99.9}$. Each configuration is presented by the x -axis (the normalized BW occupancy), the y -axis (the energy ($10\log_{10}(d_{\min}^2/2)$)), and the z -axis (the complexity (N_s)). The z -axis is illustrated using markers, where each different marker presents a particular N_s value. Since we have many configurations (25 for B_{99} and 22 for $B_{99.9}$) and some of the configurations have similar performance (energy and BW), we decided to divide the configurations into clusters based on their performance similarity. And then from each cluster, we selected only one configuration. To obtain the clusters, we applied the k -means algorithm [20, ch.14, p.509] with Euclidean distance as cost function on the configurations obtained, taking into consideration only the energy and normalized BW occupancy of each configuration. Using the k -means, we obtained four and five different clusters, respectively, for B_{99} and $B_{99.9}$. Based on the clusters obtained, we selected one configuration representing the cluster based on two conditions:

- 1) Since all configurations in the same cluster have approximately similar performance, we prioritized the complexity (N_s). Therefore, we selected the configuration with the lowest complexity as the cluster representative.
- 2) Suppose two or more configurations in the same cluster have the same minimum complexity (N_s). In that case, we select the configuration with the maximum performance, measured as $10\log_{10}(d_{\min}^2/2) - BT_b$.

In Fig. 7 and Fig. 8, the selected configurations are presented with an index number. The index number presents the row in

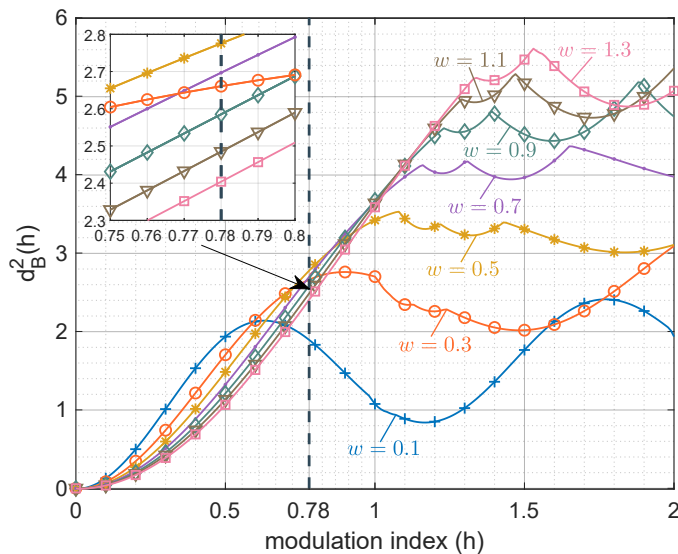


Fig. 9: Effect of pulse width w on the upper bound (d_B^2) as a function of modulation index h for binary 5SSB-FSK.

Table V and Table VI, respectively, for 99% and 99.9% normalized BW occupancy. Given later, these tables illustrate the parameters and the performance of the selected configurations. The results from these tables will be discussed in Section VI, for the sake of comparison as they are presented alongside other relevant results from other known CPM schemes.

In Fig. 8, we can see that we select only four configurations out of five, where configuration number 3 offers a remarkably better normalized BW occupancy than the configuration selected from the fourth cluster while maintaining almost the same energy performance (a slight difference of 0.1 dB). Therefore, we ignore the configuration from the cluster number 4.

VI. SIMULATION RESULTS

This section presents the results obtained based on Section III, IV, and V. As this section is dedicated to illustrate SSB-FSK performance considering many metrics varying many parameters. We have chosen to do it sequentially for the sake of simplicity. Indeed, we first evaluate each metric separately and quantify the impact of all parameters on it: error probability performance in terms of d_{\min}^2 is reported in sub-section VI-A, BER simulation is illustrated in sub-section VI-B to verify the effectiveness of d_{\min}^2 by illustrating the bit error performance of SSB-FSK signals, and power spectrum performance is depicted in subsection VI-C. Second, we start to stack metrics together and evaluate performance when considered jointly: the interplay between d_{\min}^2 and BW is presented in sub-section VI-D. By taking further the complexity into account, new tradeoffs are revealed in sub-section VI-D. Finally, when synchronization advantage is suggested through the use of exclusively integer modulation indices, simulation results are given in sub-section VI-E, demonstrating the superiority of the SSB-FSK scheme among well-known CPM schemes.

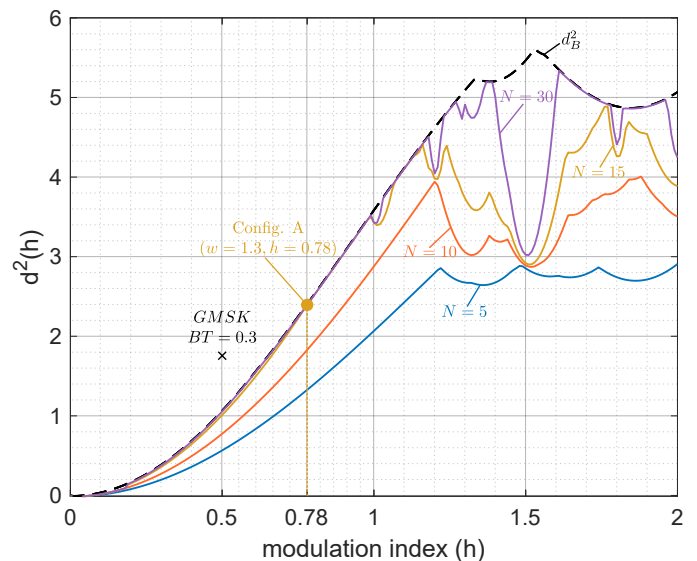


Fig. 10: Minimum normalized squared Euclidean d_{\min}^2 distance as a function of modulation index h for binary 5SSB-FSK with $w = 1.3$.

A. SSB-FSK CPM error probability Performance

The author in [1, Ch. 3] describes the effect of the parameters h, M, L on d_{\min}^2 for a variety of CPM schemes; the SSB-FSK is a pretty similar scheme compared to the ones presented in [1, Ch. 3] (*unlimited time* CPM schemes with a symmetrical form with respect to zero). However, the pulse width w is a specific parameter introduced particularly for SSB-FSK signals. Therefore, it is interesting to study its effects on the d_{\min}^2 .

Fig. 9 depicts the variations of the upper bound d_B^2 as a function of modulation index h for binary 5SSB-FSK, for pulse width $w = 0.1, 0.3, 0.5, 0.7, 0.9, 1.1, 1.3$. Consequently, we can quantify the double effect of both parameters h and w on the error probability performance of SSB-FSK, which are presented in three points:

- We obtain a better upper bound d_B^2 using a low pulse width w , e.g., $w = 0.1$ for low modulation index region h , e.g., for $h \approx 0.5$. Therefore, for small modulation index h , it is always better to use small pulse width w .
- We show that for higher modulation index h , a higher pulse width w is preferred, e.g., for $h \approx 1.5$, we obtain the best d_B^2 for $w = 1.3$. This behavior is very similar to the effect of increasing the pulse length L , which is explained in detail in [1, ch.3, p.75-76].
- In contrast to the second point, it is not always better to use higher pulse width w for higher modulation index h , where we notice that d_B^2 with $w = 0.9$ is better than $w = 1.3$, for the same $h \approx 1.9$.

Based on the previous points, we cannot draw a general trend for the effect of the pulse width w on the upper bound d_B^2 performance.

Besides, the impact of pulse width w on the upper bound d_B^2 can be seen directly from Fig. 3, where it is evident that the tails of the frequency pulse $g(t)$ go up with the increase

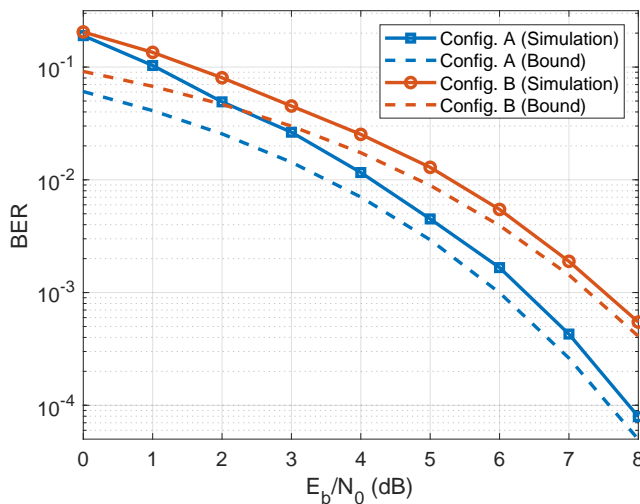


Fig. 11: BER performance of Config. A and Config. B for $M = 2$ in AWGN channel.

of pulse width w , which means an increase in inter-symbol interference (ISI). Fortunately, when the ISI is appropriately compensated at the receiver side, this can increase the redundant information (increase in memory effect). Hence, this introduces sizable gains in the upper bound d_B^2 values.

Fig. 10 illustrates the performance of minimum normalized squared Euclidean distance d_{\min}^2 as a function of h for binary 5SSB-FSK with pulse width $w = 1.3$. This configuration ($L = 5$ and $w = 1.3$) is chosen related to the *Pareto optimum* analysis results given in the previous Section (it is Config. A also given in Table III row 1). Moreover, the results are illustrated for different observation symbol intervals $N = 5, 10, 15, 30$. In addition, the GMSK is also shown as x mark, and the $d_{\min-\text{opt}}^2$ for binary B_{99} SSB-FSK (Table III row 1 or Config. A in Fig. 5) is also shown as a reference point. Fig. 10 shows that the most significant d_{\min}^2 value slightly higher than 5 can be reached, for $h = 1.61$ and $N = 30$: this is almost the absolute optimum without considering any other metric, and it is denoted by $d_{\min-\text{opt}}^2$ (this is visible in Fig. 5, it is one of the extreme points at the upper right quarter of the plane). Compared to GMSK, we obtained a gain of roughly 4.83 dB. Note that this configuration, leading to $d_{\min-\text{opt}}^2$, offers very poor *BW* performance (this is also visible in Fig. 5). That is why in Table III, we have chosen the modulation index $h = 0.78$ (Config. A), which is shown as a reference point in the figure. This result, which is different from $d_{\min-\text{opt}}^2$, is obtained because we consider the normalized bandwidth *BW* occupancy alongside the minimum normalized squared Euclidean distance d_{\min}^2 . We can notice the decrease of modulation index h (from $h = 1.61$ to $h = 0.78$), resulting in a smaller normalized bandwidth *BW* occupancy. As a consequence, the energy consumption gain compared to GMSK decreases to 1.36 dB. We can also observe that, for certain specific modulation indices h , d_{\min}^2 cannot reach the upper bound d_B^2 , especially for modulation index $h = 3/2$. This effect appears for all CPM schemes, called weak modulation indices [1, 10].

B. SSB-FSK BER

The authors in [10], [21] showed that the minimum Euclidean distance is sufficient for illustrating the performance in terms of bit error probability for a large variety of CPM schemes. Since SSB-FSK is a new CPM scheme, in this section, we present the BER simulation to verify the effectiveness of our derivations. We obtained the BER using the Viterbi algorithm, which is the optimal detector used to achieve MLSD for CPM schemes.

Fig. 11 shows the BER for Config. A and Config. B with $M = 2$. For the sake of comparison, the union bound of each configuration is also given as a dashed line. It is shown that BER curves are approaching the bounds for high SNR values, which is consistent with what we previously stated, i.e., the union bound depicts the performance of the error probability for a high SNR regime. For low SNRs, the bounds are quite loose. From Fig. 11, we can conclude that the minimum Euclidean distance d_{\min}^2 may be the right metric to adopt in order to depict the bit error probability performance.

C. SSB-FSK CPM Power Spectrum Performance

Similar to Section VI-A, the parameters' effects are already detailed for a wide variety of pulses in [1, Ch. 4]. Therefore, we present only the effect of parameter w on the PSD of the SSB-FSK signals. Moreover, in this section, we also present the effect of h on the SSB-LOSS.

Fig. 12 illustrates the PSD of binary 5SSB-FSK for different pulse width $w = 0.3, 0.7, 1.3$ as a function of the frequency, with $h = 0.78$. The choices of the parameters ($L = 5$ and $w = 1.3$) are based on the first row of Table III (Config. A in Fig. 6), also used in Fig. 9 and Fig. 10 to depict the effect of the pulse width w on the d_{\min}^2 .

In this part, we show the effect of the pulse width w on the PSD. To clarify the selection of pulse width $w = 1.3$ in our optimization solution, we added to Fig. 12 two more plots for different pulse widths $w = 0.3, 0.7$. The effect of the pulse width w on the PSD is summarized in these three points:

- Increasing w accentuates the power exponential decay of the SSB-FSK modulated signal [3].
- Increasing the pulse width w narrows the power spectral density, particularly in the frequency interval of width $1/T_s$, which is primarily evident when we compare the plots of pulse width $w = 0.3$ and the others.
- Based on the closeup figure made around $h = 0.78$ in Fig. 9, we can see that increasing w , in this particular region, does not decrease d_B^2 that much (consequently d_{\min}^2).

From these observations, it is clear that increasing the pulse width w reduces the normalized bandwidth *BW* occupancy, improves the adjacent-channel interference, and maintains approximately the same d_{\min}^2 , based on the modulation index h selected.

In general, we cannot increase the pulse width w indefinitely. For instance, from Fig. 9, we can see that increasing the pulse width w reduces d_{\min}^2 , especially for low modulation index h . Accordingly, the choice of parameters is a trade off aiming

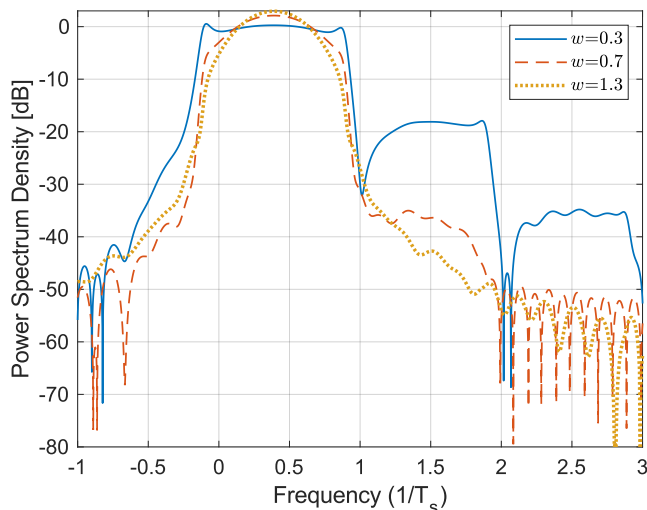


Fig. 12: Power spectral density of binary 5SSB-FSK with $h = 0.78$ and for $w = 0.3, 0.7, 1.3$

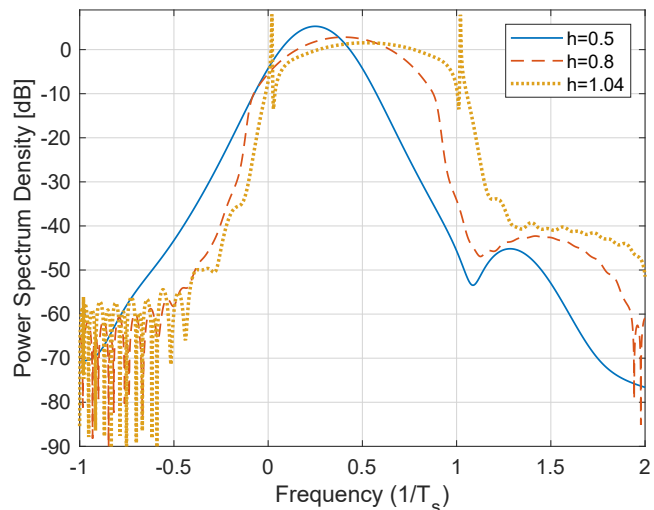


Fig. 13: Power spectral density of binary 12SSB-FSK with $w = 0.8$ and $h = 0.5, 0.8, 1.04$.

to optimize not only d_{\min}^2 , but also the normalized bandwidth BW occupancy.

Fig. 13 represents the PSD of the binary 12SSB-FSK, for $w = 0.8$ and different $h = 0.5, 0.8$ and 1.04 . In this part, we show the effect of the modulation index h on the SSB-LOSS. As in the previous part, we used the parameters obtained from the optimization Section V, i.e., the first row from Table IV, which corresponds to Config. A' in Fig. 6 (the result of the *Pareto optimum* for B_{99}). In this particular context, we notice that we obtain the lowest SSB-LOSS. It is evident that increasing the modulation index h increases the normalized bandwidth BW occupancy. It is especially visible for the frequency region between 0 and $1/T_s$. On the other hand, the modulation index h has the inverse effect on the SSB-LOSS: for $h = 0.5$, we obtain an SSB-LOSS of 2.06%, and for $h = 0.8$, the SSB-LOSS decreases to 1.63%, and then for $h = 1.04$ it reached the lowest value with an SSB-LOSS of 0.366%. However, for different parameters, e.g., 6SSB-FSK and pulse width $w = 0.37$, increasing the modulation index will increase the SSB-LOSS. Therefore, it is impossible to generalize the effect of the modulation index h on the SSB-LOSS. Otherwise, it is always true that taking an integer modulation index h will reduce the SSB-LOSS; this decrease is due to the spectral lines, which take a part of the transmitted power. This observation is due to selecting a modulation index h around an integer (≈ 1). Even if these spikes seem undesirable because a part of the transmitted power is wasted, they could be of great interest for synchronization purposes [1, Ch. 9, Sec. 1][22].

D. Single-Sideband CPM Energy-Bandwidth Comparison

In this section, through Fig. 14 and Fig. 15, we show comparison plots between SSB-FSK and other CPM schemes. We used SSB-FSK parameters based on the results obtained from the optimization study given in Section V. The plots are characterized by the SSB normalized bandwidth occupancy in the x-axis (BW) and $10 \log_{10}(d_{\min}^2/2)$ for the y-axis (en-

ergy). Moreover, we divided this section into two parts; one illustrates the occupied BW as 99% of the power inside BT_b . The other illustrates 99.9% of the power in the BT_b (Note that the 99.9% is a more significant measure compared to the 99%; therefore, 99.9% curves and configurations are located on the right side compared to 99%). The curves and configurations with better performance are located toward the upper left side. For each BW part, we will always start with a general comparison between the optimum curves obtained for SSB-FSK and those obtained for CPM schemes, where the optimum curves do not consider the complexity (N_s). Then, we move on to a more detailed comparison, where we also consider the configurations with optimized complexity and evaluate how much they are biased from the optimum curves. The optimum curves for SSB-FSK are the same *Pareto optimum* curves obtained from Section V-C, and they are presented with the same notation $P_{\text{opt-max}}$, followed by the modulation level M (e.g., $P_{\text{opt-max-4}}$, for $M = 4$). For each of the optimum curves, the optimum normalized minimum squared Euclidean distance $d_{\min-\text{opt}}^2$ and the optimum normalized bandwidth BW occupancy BW_{opt} are also presented in the plots, denoted by Config. A and Config. B for B_{99} , respectively. Likewise, they will be denoted by Config. A' and Config. B' for $B_{99.9}$. A subscription is used to refer to the modulation level, e.g., Config. A₂ refers to Config. A for the binary case.

A next step in the following discussion is to include the complexity as a third performance metric along side the energy efficiency and the bandwidth occupancy in order to be able to select efficient SSB-FSK schemes with reasonable receiver complexity. Therefore, we chose to superimpose the configurations obtained from Section V-D (by taking into account the metric N_s), presented as triangular markers with an index number, to *Pareto optimum* curves. Similar to Section V-D, the index number presents the row in Table V and Table VI, for 99% and 99.9% normalized BW occupancy, respectively. For a fair comparison with other CPM schemes, we present the RC curves for different modulation levels M and pulse

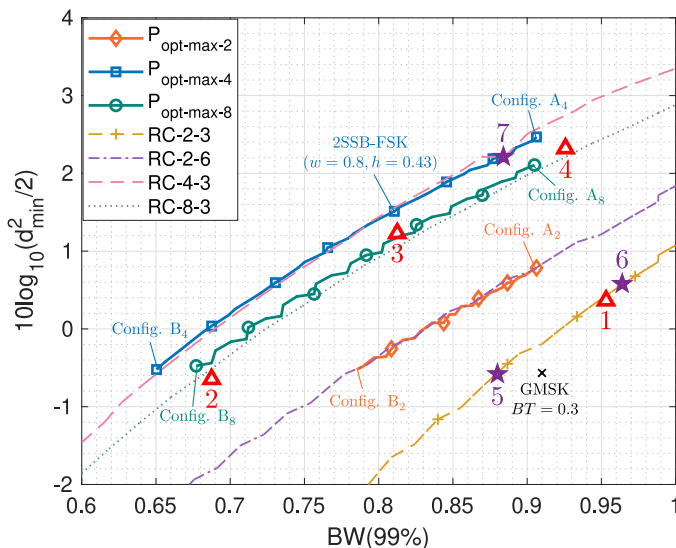


Fig. 14: Energy-Bandwidth plot for LSSB-FSK and LRC for different modulation level $M = 2, 4, 8$ using B_{99} . GMSK is presented as an “x” mark.

lengths L . The legends of the RC-based schemes are given starting with the pulse type followed by the modulation level M and the pulse length L (e.g., RC-2-3 is the raised cosine pulse for modulation level $M = 2$ and pulse length $L = 3$). For the RC curve, we also present the configurations with $N_s < 64$ (similar to Section V-D, configurations with $N_s > 64$ are considered as highly complex systems).

Each configuration relative to the RC pulse is shown as star marker with an index number. Similar to SSB-FSK, the index number presents the row in Table V and Table VI, respectively, for 99% and 99.9% normalized BW occupancy. Finally, the configuration of GMSK with $BT = 0.3$ is also shown as an “X” marker in Fig. 14 and Fig. 15. The GMSK has a complexity $N_s = 16$.

Note, all configurations located outside the region of the energy-bandwidth comparison are not considered (y -axis < -2 dB for 99% and 99.9%, the x -axis > 1 and > 1.25 for 99% and 99.9%, respectively). Therefore, we can observe that there are no configuration for some of the RC curve.

1) 99% Bandwidth occupancy: Fig. 14 illustrates the performance for B_{99} of SSB-FSK signals compared to LRC for different modulation levels M . Starting with the SSB-FSK curves, the $P_{\text{opt-max}}$ for all modulation levels M outperforms the GMSK, where we obtain an energy consumption gain of 1.35, 3.03, and 2.67 dB for Config. A_2 , Config. A_4 , and Config. A_8 for approximately the same normalized bandwidth BW occupancy, respectively. Similarly, we obtain a normalized bandwidth BW occupancy gain of 0.125, 0.26, and 0.233 for Config. B_2 , Config. B_4 , and Config. B_8 for almost the same energy consumption, respectively. Compared to the binary RC, the $P_{\text{opt-max-2}}$ outperforms the binary 3RC; however, we obtain the same performance compared to binary 6RC. On the other hand, the $P_{\text{opt-max-4}}$ and $P_{\text{opt-max-8}}$ outrun the binary RC for all cases. Likewise, for $M = 4$, using the $P_{\text{opt-max-4}}$, we obtain almost the same performance as quaternary 3RC.

TABLE V:

Performance of LSSB-FSK and LRC configurations with the lowest complexity for 99% normalized BW occupancy.

Index	Modulation Type	d_{min}^2	BW	States (N_s)
1	1SSB-FSK ($M = 8, h = 0.25, w = 0.7$)	2.175	0.953	4
2	2SSB-FSK ($M = 8, h = 0.25, w = 0.5$)	1.724	0.687	32
3	2SSB-FSK ($M = 4, h = 0.4, w = 0.5$)	2.654	0.8125	20
4	2SSB-FSK ($M = 4, h = 0.5, w = 1$)	3.412	0.925	8
5	3RC ($M = 2, h = 0.5$)	1.75	0.88	16
6	3RC ($M = 2, h = 0.6$)	2.286	0.964	40
7	3RC ($M = 2, h = 0.5$)	3.33	0.884	64

Worst

Best

Similarly, for $M = 8$, we obtain a slightly better performance using $P_{\text{opt-max-8}}$ compared to 8-ary 3RC. However, for all normalized bandwidth occupancies, the $P_{\text{opt-max-4}}$ outperforms the $P_{\text{opt-max-8}}$, meaning that increasing the modulation level M will not always increase the performance. Besides, we can highlight the effect of increasing the modulation level M , especially between $M = 2$ and $M = 4$; we obtain an energy consumption gain of 1.68 dB between Config. A_2 and Config. A_4 for the same normalized bandwidth occupancy. Similarly, considering now the normalized bandwidth occupancy, we obtain a gain of 0.135 between Config. B_2 and Config. B_4 for almost the same energy consumption.

When the complexity is taken into account inside our configurations selection process, a more intelligible reading of Fig. 14 is given through Table V. It is clear that configurations “4” (2SSB-FSK) and “7” (3RC) have the highest energy performance, where configuration “4” (2SSB-FSK) is slightly better in terms of energy performance. From a bandwidth occupancy point of view, apart from configuration “2” (2SSB-FSK), which is clearly distinguished by the lowest normalized BW occupancy, all other configurations perform pretty similarly. From a complexity point of view, configurations “1” (1SSB-FSK) and “4” (2SSB-FSK) stand out by offering the optimal detection with the lowest number of states. Configuration “1” (1SSB-FSK) has lower complexity ($N_s = 4$) compared to configuration “4” (1SSB-FSK) ($N_s = 8$) at the price of a vast decrease in the energy efficiency. Finally, if we consider all performance metrics together, it is evident from Table V, that configuration “4” (1SSB-FSK) presents the best tradeoff.

Overall, these comparisons reveal that if we consider each metric alone (energy, normalized BW occupancy, receiver complexity) or consider all metrics together, we will always obtain the best configuration from the SSB-FSK scheme.

2) 99.9% Bandwidth occupancy: As in the previous part, in Fig. 15, we compare SSB-FSK $P_{\text{opt-max}}$ curves with GMSK (shown as x mark in the plot). We achieve a gain of 2.8 dB, 2.3 dB, and 2.4 dB for Config. A'_2 , Config. A'_4 , and Config. A'_8 , respectively, at nearly the same normalized bandwidth BW

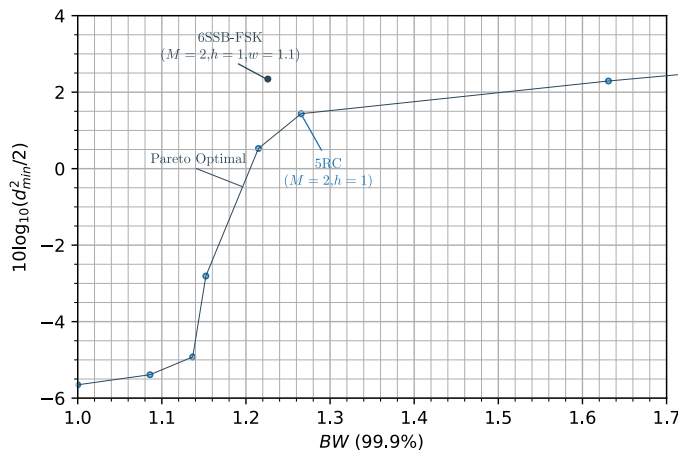


Fig. 16: *Pareto optimum* plot of RC with modulation index $h = 1$ in comparison to configuration “4” for B_{999} .

that configuration “4” (6SSB-FSK) presents a gain of 0.9 dB and slightly lower normalized BW occupancy 0.04 compared to the best configuration presented in the *Pareto optimum* for RC ($L = 5$, $M = 4$, $h = 1$). In terms of complexity, the two configurations have the same number of state $N_s = 32$. Note that, all configurations shown on the *Pareto optimum* curve (other than the selected configuration of RC) have $N_s > 128$ except the first configuration located at the lower-left corner has a $N_s = 2$ (at the expense of poor performance).

VII. CONCLUDING REMARKS AND DESIGN DIRECTIVES

We have selected the best parameter combinations from the optimization methods to obtain the optimal performance of the SSB-FSK scheme. Based on the parameters chosen from the optimization solution, we achieved a better spectrum occupancy, a gain in error probability performance, and a massive decrease in complexity compared to the original SSB-FSK proposal [2, 8]. Our optimization method leads to practical tradeoffs through certain parameter combinations. These tradeoffs differ because they prioritize performance metrics differently. The choice depends on the target application and, consequently, the resources we want to allocate. Finally, we have applied an energy-bandwidth comparison, where we achieved a similar or better performance compared to certain robust CPM modulations. In general, the SSB-FSK has the advantage of being more flexible than RC. For instance, it has been proven that this new waveform is highly tunable, able to provide the most suitable configuration responding to the designer requirements (energy, bandwidth, or complexity). In the B_{99} case, we showed that the configurations obtained from SSB-FSK modulation outperform the RC and GMSK in energy-bandwidth and receiver complexity in any position in the defined comparison region. It is always possible to find a SSB-FSK configuration that outperforms the RC. For B_{999} , the answer cannot be binary or clear-cut, but a more nuanced analysis has been made, offering several possible tradeoffs. Nevertheless, the B_{999} analysis allows us to define one SSB-FSK configuration combining excellent performance and advantage in synchronization since it operated with an integer

modulation index. This, in particular, offers to SSB-FSK scheme the potential to go beyond what has been achieved with well known CPM schemes (e.g., RC and GMSK). Moreover, we showed that using an integer h with RC will never exceed the SSB-FSK results. Overall, it is clear that the SSB-FSK is not always the best scheme, and it heavily depends on the parameters. Therefore, selecting the best CPM schemes heavily relies on the target application.

VIII. CONCLUSION

In this paper, we have investigated a CPM scheme that can directly generate a SSB spectrum. To exploit all its potential, we investigated the error probability based on the derivation of the minimum Euclidean distance as a function of the modulation index, pulse width, and pulse length. We explored the spectrum of SSB-FSK by quantifying its signal power bandwidth occupancy using a numerical method. We addressed the receiver complexity aspects. These metrics have been used in two different optimization methods to illustrate the full potential of this waveform alongside well-known CPM schemes. Future work will focus on the sub-optimum Viterbi-based demodulation scheme using pulse amplitude modulation (PAM) decomposition to offer more sizable complexity reduction. The aim will be to explore other possible configurations offering further possible gains to go beyond what has been achieved with well-known CPM schemes.

APPENDIX A

In this appendix, we detail how (9) was obtained from (8), similarly to the derivation given in [1, ch.2, p.26-p.28] and [12, ch.4, p.251-p.252]. The carrier modulated signal corresponding to the real part of (1) is expressed as

$$s(t, \alpha) = \sqrt{\frac{2E}{T_s}} \cos[w_0 t + \phi(t; \alpha)] \quad (26)$$

where $E_s = 2E$ is the energy per transmitted symbol and w_0 is the carrier frequency. To simplify the derivation, the carrier frequency w_0 is assumed much larger than $2\pi/T_s$. We suppose that the two signals $s(t, \alpha_i)$ and $s(t, \alpha_j)$ differ over an interval N . The Euclidean distance between the two signals over the interval N is defined as [12]

$$\begin{aligned} & \int_0^{NT_s} [s(t, \alpha_i) - s(t, \alpha_j)]^2 dt = \\ & \int_0^{NT_s} s(t, \alpha_i)^2 dt + \int_0^{NT_s} s(t, \alpha_j)^2 dt \\ & - 2 \int_0^{NT_s} s(t, \alpha_i) s(t, \alpha_j) dt. \end{aligned} \quad (27)$$

Since both signals are constant envelope with energy E over an interval T_s (we obtain E by integrating the square of (26) over an interval T_s), the second line of (27) can be expressed as

$$\int_0^{NT_s} s(t, \alpha_i)^2 dt + \int_0^{NT_s} s(t, \alpha_j)^2 dt = 2NE. \quad (28)$$

Using the trigonometric function $\cos(a)\cos(b) = \frac{1}{2}(\cos(a-b) + \cos(a+b))$ and assuming large carrier frequency, the third line in (27) can be presented as

$$2 \int_0^{NT_s} s(t, \alpha_i) s(t, \alpha_j) dt = 2 \frac{2E}{T_s} \int_0^{NT_s} \cos[w_0 t + \phi(t; \alpha_i)] \cos[w_0 t + \phi(t; \alpha_j)] dt = \frac{2E}{T_s} \int_0^{NT_s} \cos[\phi(t; \alpha_i) - \phi(t; \alpha_j)] dt. \quad (29)$$

From (28) and (29), we can present (27) in the form

$$2NE - \frac{2E}{T_s} \int_0^{NT_s} \cos\Delta\phi(t) dt, \quad (30)$$

where $\Delta\phi(t)$ denotes the phase difference between the two signals. Here E is the energy obtained for an interval and not for a data bit. Therefore, for a fair comparison between many modulation schemes with different modulation levels M , E has to be normalized to obtain the energy per data bit E_b . The normalization of E is defined as

$$E = \log_2 M E_b. \quad (31)$$

Placing (30) and (31) in (8), we obtain (9).

REFERENCES

- [1] J. B. Anderson, T. Aulin, and C.-E. Sundberg, *Digital phase modulation*. Springer Science & Business Media, 2013.
- [2] H. Farès, D. C. Glattli, Y. Louet, J. Palicot, C. Moy, and P. Roulleau, "From quantum physics to digital communication: Single sideband continuous phase modulation," *Comptes Rendus de l'Académie des Sciences des Physiques*, vol. 19, no. 1-2, pp. 54–63, 2018.
- [3] H. Farès, D. C. Glattli, Y. Louet, J. Palicot, P. Roulleau, and C. Moy, "Power spectrum density of single side band cpm using lorentzian frequency pulses," *IEEE Wireless Communications letters*, vol. 6, no. 6, pp. 786–789, 2017.
- [4] D. Glattli and P. Roulleau, "patent wo2016124841 a1," 2016.
- [5] L. S. Levitov, H. Lee, and G. B. Lesovik, "Electron counting statistics and coherent states of electric current," *Journal of Mathematical Physics*, vol. 37, no. 10, pp. 4845–4866, 1996.
- [6] J. Dubois, T. Jullien, F. Portier, P. Roche, A. Cavanna, Y. Jin, W. Wegscheider, P. Roulleau, and D. Glattli, "Minimal-excitation states for electron quantum optics using levitons," *Nature*, vol. 502, no. 7473, p. 659, 2013.
- [7] T. Jullien, P. Roulleau, B. Roche, A. Cavanna, Y. Jin, and D. Glattli, "Quantum tomography of an electron," *Nature*, vol. 514, no. 7524, p. 603, 2014.
- [8] H. Farès, C. Glattli, Y. Louët, C. Moy, J. Palicot, and P. Roulleau, "New binary single side band cpm," *2017 24th International Conference on Telecommunications (ICT)*, pp. 1–5, May 2017.
- [9] G. D. Forney, "The viterbi algorithm," *Proceedings of the IEEE*, vol. 61, no. 3, pp. 268–278, March 1973.

- [10] T. Aulin, N. Rydbeck, and C.-E. Sundberg, "Continuous phase modulation-part ii: Partial response signaling," *IEEE Transactions on Communications*, vol. 29, no. 3, pp. 210–225, 1981.
- [11] T. Aulin and C. Sundberg, "An easy way to calculate power spectra for digital fm," *IEE Proceedings F - Communications, Radar and Signal Processing*, vol. 130, no. 6, pp. 519–526, October 1983.
- [12] J. G. Proakis and M. Salehi, *Digital communications*. McGraw-hill New York, 2008, vol. 4.
- [13] L. Greenstein, "Spectra of psk signals with overlapping baseband pulses," *IEEE Transactions on Communications*, vol. 25, no. 5, pp. 523–530, 1977.
- [14] R. H. H. Yang, C. K. Lee, and S. J. Chern, "Continuous phase modulation (CPM) revisited: Using time-limited phase shaping pulses," *IEICE Transactions on Communications*, vol. E96-B, no. 11, pp. 2828–2839, 2013.
- [15] M. Messai, K. Amis, and F. Guilloud, "On the Optimization of a PSP-Based CPM Detection," *IEEE Transactions on Wireless Communications*, vol. 15, no. 3, pp. 2144–2154, 2016.
- [16] A. Syed, "Comparison of noncoherent detectors for sqpsk and gmsk in phase noise channels." International Foundation for Telemetry, 2007.
- [17] E. S. Perrins, "Reduced Complexity Detection Methods for Continuous Phase Modulation," 2005.
- [18] R. T. Marler and J. S. Arora, "Survey of multi-objective optimization methods for engineering," *Structural and multidisciplinary optimization*, vol. 26, no. 6, pp. 369–395, 2004.
- [19] P. Ngatchou, A. Zarei, and A. El-Sharkawi, "Pareto multi objective optimization," *Proceedings of the 13th International Conference on Intelligent Systems Application to Power Systems*, pp. 84–91, Nov 2005.
- [20] T. Hastie, R. Tibshirani, and J. Friedman, *The elements of statistical learning: data mining, inference, and prediction*. Springer Science & Business Media, 2009.
- [21] T. Aulin, "Symbol error probability bounds for coherently viterbi detected continuous phase modulated signals," *IEEE Transactions on Communications*, vol. 29, no. 11, pp. 1707–1715, 1981.
- [22] Z. Xu and Q. Wang, "Autocorrelation Function of Full-Response CPM Signals and Its Application to Synchronization," *IEEE Access*, vol. 7, pp. 133 781–133 786, 2019.



Karim Kassin was born in Lebanon, Kalamoun, in 1995. He received the B.S. degree in Communications and Electronics engineering from Beirut Arab University (BAU) in 2017. He received the M. Sc in Telecommunications engineering from INSA Rennes in 2018. He is currently pursuing a Ph.D. in signal processing and communication systems at Centrale-Supélec, France. His research interests include digital communication theory, wireless communications, synchronization, channel coding, spectrally efficient systems, and complexity reduction receivers.



Haïfa Farès is an associate professor at Centrale-Supélec of Rennes and member of the Signal Communication Embedded Electronics Research Group, Institute of Electronics and Telecommunications, Rennes Lab (CNRS). She received the bachelor and the M.Sc. degrees in Telecommunication Engineering from the Higher School of Communications of Tunis (Sup'Com), in 2007 and 2008, respectively. She was awarded the best student engineering project in 2007. She received the Ph.D. degree in digital communications from IMT-Atlantique,

France, in 2011. Her research interests are in the area of Communication Theory, including nonlinear modulations, green communications, iterative decoding algorithms and non-orthogonal multiple access.



Yves Louët received his Ph.D. degree in digital communications from Rennes University, France, in 2000. The topic of his Ph.D. thesis regarded peak to average power reduction in OFDM modulation with channel coding. He was a Research Engineer in 2000 with SIRADEL Company, Rennes, and involved in channel propagation modelling for cell planning. He was involved in French collaborative research projects, including COMMINDOR, ERASME, and ERMITAGES about channel modelling in many frequency bands, especially, 60 and 5 GHz for further

telecommunication systems. In 2002, he joined Supélec as an Associate Professor. His teaching and research activities were in line with signal processing and digital communications applied to software and cognitive radio systems. He was involved in many collaborative European projects, including FP7E2R, CELTIC B21C, CELTIC SHARING, NoE Newcom, and COST and French projects, including ANR PROFIL, ANR INFOP, WONG5, FUI AMBRUN, APOGEES, TEPN, and WINOCOD. His research contribution is mainly focused on new waveforms design for green cognitive radio and energy efficiency enhancement. In 2010, he got his research habilitation (HDR) from Rennes University and became Full Professor with Supélec and later CentraleSupélec. He is the Head of the Signal Communication Embedded Electronics Research Group, a team from the CNRS Institute of Electronics and Telecommunications of Rennes Lab, and the President of the URSI Commission C.



Christian Glattli research Director at CEA, born in 1954, State Ph-D in 1986 Orsay, is head of of the Nanoelectronic group (from 1994 to 2018) at the CEA Saclay France. He has also founded the Mesoscopic Physics group at the Ecole Normale Supérieure, Paris, in 2000 (lead from 2000 to 20012). His main achievements are : novel techniques for noise measurements in solids leading to the experimental observation of fractional charge carriers (1999 EuroPhysics PRIZE, 1997 Ancel Prize French Physical Society, 1998 Silver Medal CNRS);

the Development of Single Electron Sources (Science 2007) for Flying Qubits in Electron Quantum Optics with the discovery of Levitons (Nature 2013) enabling Electron Quantum State Tomography (Nature 2014); the measurement of the Josephson Frequency of $e/3$ and $e/5$ anyon charges (SCIENCE 2019). After the discovery of leviton quantum waves, he applied the leviton principle to classical Hertzian waves for digital communications : patent WO2016124841A1 .